PERGAMON

International Journal of Solids and Structures 37 (2000) 4893–4913

INTERNATIONAL JOURNAL OF SOLIDS and STRUCTURES

www.elsevier.com/locate/ijsolstr

Enhanced ballistic performance of confined multi-layered ceramic targets against long rod penetrators through interface defeat

H.D. Espinosa [a,*,1], N.S. Brar [a,b], G. Yuan [a], Y. Xu [a], V. Arrieta [a]

[a] *School of Aeronautics and Astronautics, Purdue University, West Lafayette, IN 47907-1282, USA*
[b] *Impact Physics Laboratory, University of Dayton Research Institute, Dayton, OH 45469-0182, USA*

Received 19 June 1998; in revised form 2 July 1999

Abstract

Impact recovery experiments on confined multi-layered ceramic targets are performed to identify materials and structural design issues in interface defeat of long rod tungsten heavy alloy (WHA) penetrators. In-situ stress measurements are made, with embedded manganin/constantan gauges, and velocity histories of the target rear surface are measured using an interferometric technique. Material response to penetration is examined by considering different hardness of the cover steel plate and two types of ceramics, viz., Alumina and TiB_2. The combined material-structural response is examined by changing the thickness of the graphite plate, used to accommodate the deforming WHA penetrator, and by welding top and bottom plates with the middle plate to increase the stiffness of the assembled multi-layered target. In total, eight shots are performed in the velocity range of 1.5–1.7 km/s. Ceramic damage is studied by quantifying the size and distribution of fragments in recovered sample. SEM and optical microscopy performed on recovered ceramic plates show that microcracking is the dominant failure mode in multi-layered ceramic targets. Crack surface area per unit volume is estimated, on cross sections of the ceramic targets along several orientations. Correlation between axial stress and crack density is investigated. Examination of the post-shot multi-layered ceramic targets revealed complete and partial interface defeat of long rod tungsten heavy alloy penetrators. Targets with extra stiffness, on account of weld and larger bottom plate thickness, achieved complete defeat of the penetrator.

Keywords: Ballistic penetration; Damage; Fragmentation; Interferometry; Fracture; Plasticity

* Corresponding author. Fax: +1-765-494-0307.
E-mail address: espinosa@ecn.purdue.edu (H.D. Espinosa).
[1] http://roger.ecn.purdue.edu/~espinosa.

0020-7683/00/$ - see front matter
PII: S0020-7683(99)00196-1

1. Introduction

There have been a number of investigations to utilize the high compressive strength and low density properties of ceramics for designing light-weight armor (see e.g. Hauver et al., 1993, 1994; Rapacki et al., 1996, Bless et al., 1992). Shockey et al. (1990) studied the type and extent of damage as a result of long rod penetration in ceramic targets prepared with the depth of penetration (DOP) configuration. They postulated that penetration occurs only if the comminuted material in front of the penetrator nose flows laterally under high pressure. A statistical analysis of the size and shape of fragments and of various types of cracks was carried out from the recovered ceramics in shot targets. Furthermore, these observations suggested that ceramic internal friction is one of the most important material properties that influence its ballistic performance and motivated a number of pressure-shear studies on intact ceramics and ceramic powders (see e.g. Klopp and Shockey, 1991; Espinosa and Clifton, 1991; Sairam and Clifton, 1994).

A detailed experimental study to design effective multi-layered ballistic targets containing ceramic plates or disks is due to Hauver et al. (1993, 1994) and Rapacki et al. (1996). It was concluded from the results of these studies that the ballistic resistance of a particular ceramic to long rod penetration is not unique; it depends very strongly on the nature of ceramic confinement and configuration of the multi-layered target. Furthermore, it was demonstrated that ballistic efficiency of a confined ceramic diminishes with the extent of penetration of a long rod into the ceramic. They extended the interface defeat study by Bless et al. (1992), by configuring the multi-layered ceramic targets in order to completely defeat the tungsten heavy alloy (WHA) long rod penetrators at the ceramic-cover plate interface. A thin plate of graphite at the interface between the confined ceramic and cover plate was added by Hauver et al. (1993, 1994). This plate appeared to assist shear localization of the WHA penetrator at the cover plate-ceramic interface. Lateral flow of the penetrator at the graphite–ceramic interface was observed by Hauver et al. (1993, 1994). Optical observations on the recovered ceramic tiles, from post-shot targets, showed very little damage. They concluded that ceramic damage during the ballistic penetration event could be minimized if it is configured with optimum confinement in a multi-layered target.

The challenge of developing effective ceramic armor systems still remains. Moreover, a clear understanding of the role of the various components in a multi-layered target system is lacking. The approach of combining experimental and computational studies to design an armor system for a specific ballistic threat is finding more acceptance among various groups. However, implementation of an iterative computational/experimental procedure requires reliable material models incorporating microfailure and macrofracture of ceramics, steels, titanium alloys, and penetrator materials. In this paper, a systematic study on the effect of target stiffness, cover plate hardness, graphite layer thickness, back plate thickness, and ceramic material is performed. Damage mechanisms in impacted confined alumina and TiB_2 multi-layered target plates penetrated by WHA long rods are examined. The deformation behavior of WHA penetrator at the ceramic cover-plate interface is examined using optical microscopy. Number and size of cracks and fragments in recovered ceramic targets is computed as a function of position relative to the penetrator cavity. Crack surface area per unit volume on different orientations is evaluated by stereographic analyses. Furthermore, in-material stress measurements and back surface velocity histories during ballistic penetration are reported.

2. Experimental method

2.1. Materials

Cercom of Vista, CA supplied alumina (Ebon-A) and TiB_2 ceramic disks, 72 mm in diameter and 25 mm thick. Densities of alumina and TiB_2 were 3.97 and 4.5 g/cm^3, respectively.

2.2. Target configuration and assembly

A total of eight ballistic targets were configured and assembled following the penetrator interface defeat target geometry of Hauver et al. (1994). Configuration and various steps followed in assembling each target are described below.

2.2.1. Targets 7-1797 and 7-1798

These targets consisted of three plates, as shown schematically in Fig. 1. The top 25.4 mm thick 150 mm in diameter 4340 steel cover plate was machined on the bottom to accept a 2.4 mm thick and 73 mm in diameter graphite disk. The middle disk consisted of 25 mm thick and 72 mm in diameter Cercom ceramic disk (Ebon-A alumina in 7-1797 and TiB_2 in 7-1798) shrink fitted in a 8 mm wide 17-4 PH steel ring. A shrink fit temperature of 900 F was used to achieve a radial pre-stress of 100 MPa (Hauver, 1997). The steel ring was further shrink fitted into a 25.5 mm thick 150 mm in diameter 4340 steel ring. The bottom plate was 25 mm thick 4340 steel plate. Both the faces of the ceramic containing steel plate, the lower face of the top steel plate, and the upper face of the bottom plate were lapped to ascertain flatness at the interfaces. Two Dynasen stress/strain gauges, Manganin/Constantan gauges, one on top of the Ebon-A alumina ceramic and another on top of the bottom 4340 steel plate, were glued to record the stress/strain histories during the penetration process. The three plates were bolted together on

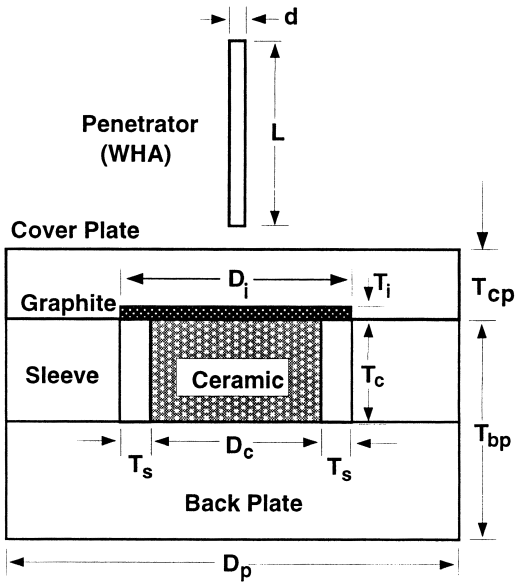

Fig. 1. Schematic of targets 7-1797 and 7-1798.

the periphery using 12 equally spaced grade-8 bolts. A shock attenuator block, consisting of 24 alternate sheets of 0.8 mm thick 2024-aluminum and plastic, was glued on top of the target assembly. A VISAR was set up to measure the free surface motion of the back steel plate as shown in Fig. 2. The bottom surface of the cover plate with the embedded graphite plate is shown in Fig. 3. The top surface of the ceramic plate with the double ring assembly is shown in Fig. 4.

2.2.2. Targets 7-1799, 7-1800, and 7-1801

The cover, middle, and bottom plates of these targets were prepared in exactly the same way as in 7-1797 with the exception that the graphite disk in 7-1801 was only half as thick. The three plates were assembled using 12 equally spaced grade-8 bolts without any stress/strain gauges at the two interfaces, between the top plate and upper surface of ceramic and between the bottom plate and lower surface of the ceramic. The rigidity of the assembled target was enhanced by welding the cover plate to the middle plate and the bottom plate to the middle plate along 45° grooves, machined at the periphery of the two interfaces, as shown in Fig. 5. The welding for targets 7-1799 and 7-1800 was carried out at Purdue University, whereas target 7-1801 was welded at the University of Dayton Research Institute (UDRI). In all cases, the 45° grooves were filled with the weld material. Cover plate hardness, type of ceramic in these targets, and other target parameters are summarized in Table 1.

2.2.3. Targets 7-1802 and 7-1803

The cover, middle, and bottom plates of these targets were prepared in exactly the same way as in 7-1797. Both the targets contained TiB_2 ceramic disks. The Rockwell Hardness of the cover plate was 35, in target 7-1802, whereas it was 53 in target 7-1803. The intent was to determine the effect of the cover plate hardness on the ballistic performance of the target. The three plates were assembled using 12

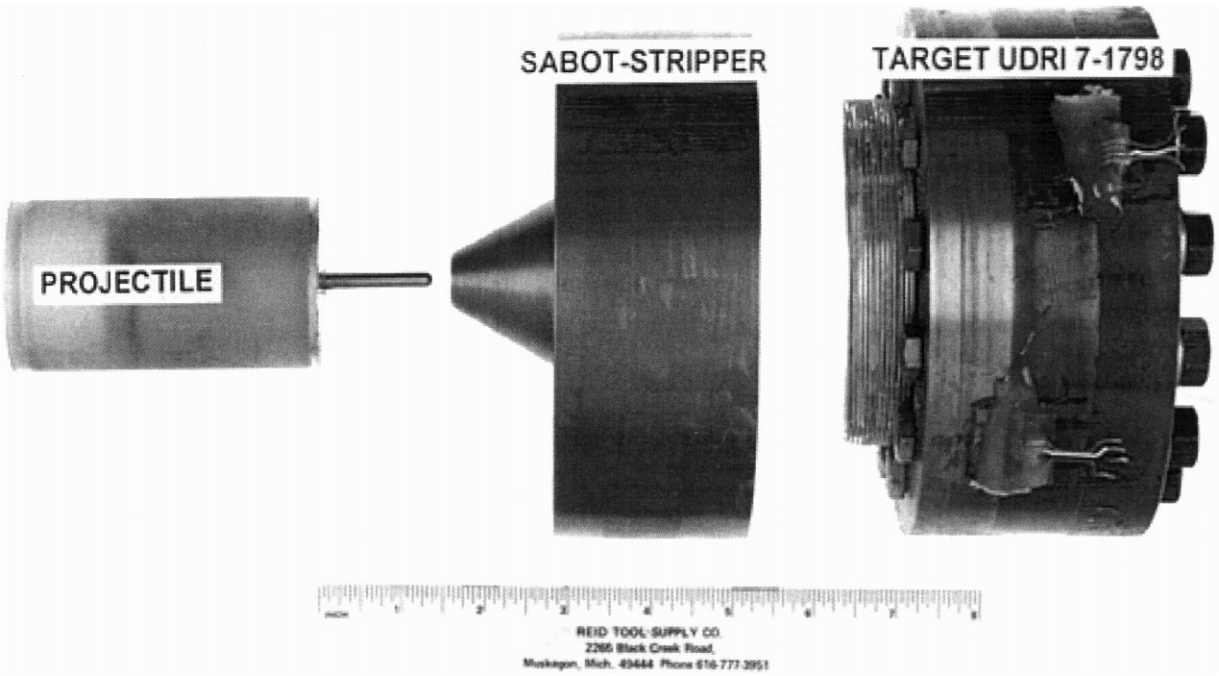

Fig. 2. Photograph showing projectile, sabot stripper, and multi-layered target.

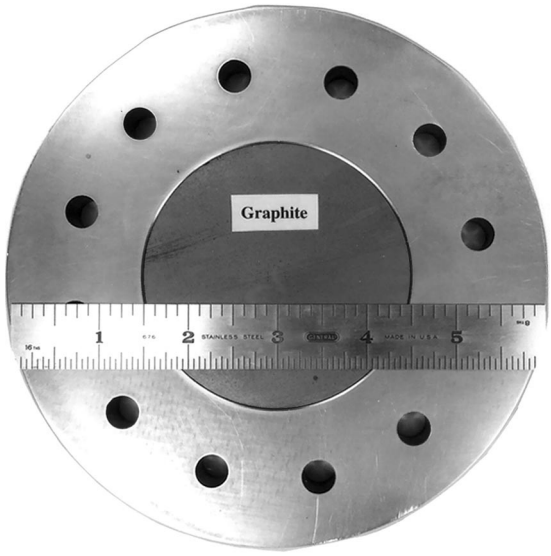

Fig. 3. Photograph of cover plate with graphite disk prior to the experiment.

grade-8 bolts with a stress/strain gauge embedded at the interface between the bottom of the ceramic and the upper surface of the steel bottom plate. The rigidity of the assembled target was enhanced by welding only the cover plate to the middle plate along the 45° groove machined at the top interface. The welding was performed at UDRI by completely filling the groove.

2.2.4. Target 7-1804

The configuration and the target cover and middle plates were prepared in exactly the same way as in 7-1797. The bottom plate was only 19 mm thick instead of 25 mm used in all the other targets. The

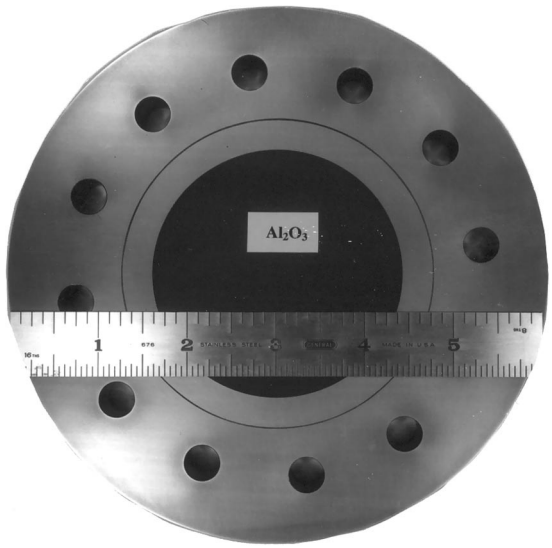

Fig. 4. Photograph of TiB_2 ceramic disk with the two steel rings after shrink fitting.

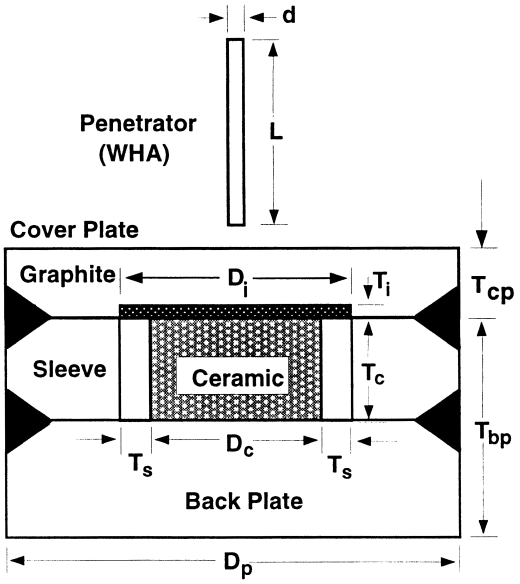

Fig. 5. Schematic of targets 7-1799, 7-1800, and 7-1801.

intent was to evaluate the effect of reducing the thickness of the bottom plate on the ballistic performance of the target. The Ebon A Alumina ceramic disk was contained in the middle plate. The hardness of the cover plate was $Rc = 52$. The cover plate was welded to the middle plate and the bottom plate to the middle plate along the 45° grooves, machined on the periphery at the two interfaces, as shown in Fig. 5. The welding was performed at UDRI and the weld material filled only 1/3 of the groove. The various target configurations are summarized in Table 1.

2.3. Ballistic experiments

Penetrator rods for the first four shots were machined from Teledyne X21 93% tungsten stock similar to that used by Hauver et al. (1993, 1994). Shots 7-1797, 7-1798, 7-1799, and 7-1800 were performed

Table 1
Summary of target configurations

Shot no.	Ceramic[a]	Cover plate hardness	Graphite thickness (mm)	Stress/strain gauge at interface 1	Stress/strain gauge at interface 2	Weld/ interface 1	Weld/ interface 2
7-1797	Ebon-A $Al_2 2O_3$	35	2.37	Yes	Yes	No	No
7-1798	TiB_2	35	2.39	Yes	Yes	No	No
7-1799	Ebon-A Al_2O_3	53	2.38	No	No	Yes	Yes
7-1800	TiB_2	54	2.37	No	No	Yes	Yes
7-1801	Ebon-A Al_2O_3	52	1.3	No	No	Yes	Yes
7-1802	TiB_2	30	2.41	No	Yes	Yes	No
7-1803	TiB_2	51	2.4	No	Yes	Yes	No
7-1804	Ebon-A Al_2O_3	51	2.4	No	No	Yes	Yes

[a] Nominal thickness and diameter of Ebon-A Al_2O3 and TiB_2 ceramic disks were 25 and 72 mm.

with $L/D = 20$ penetrators ($D = 4.93$ mm). Tungsten penetrators with the same dimensions as used in shots 7-1797 to 7-1800 for the last four shots were obtained from the Army Research Laboratory. Lexan sabots used to launch the penetrators were stripped using a specially designed sabot stripper as shown in Fig. 2. The shots were performed using a 50 mm powder gun at UDRI. The shot data is summarized in Table 2. Normal impact was used in all shots in view of the fact that oblique impact represents an easier problem for interface defeat. The outputs of the stress/strain gauges were recorded using a Dynasen pulsed power supply. Strain and stress values were determined following Dynasen data reduction procedure (Charest, 1997).

2.4. Fragment and macrocrack distribution in ceramics

The plates in each post-shot target were carefully separated. A two-component epoxy was poured into the crater/cavity made by the penetrator to keep the fragmented ceramic intact for sectioning and subsequent analysis. Fragmented ceramic target disks were sectioned on a plane containing the impact direction. Crack patterns were examined to determine failure mechanisms and to quantify crack surface area per unit volume. Microcrack surface area per unit volume was estimated by equating the total crack surface area per unit volume, S_v, to twice the average value of the number of intersections of a set of test lines of unit length, P_L. In other words, $P_L =$ Number of intersections/(Number of lines $\times$ Length of each line/Magnification) (see e.g. Pellisier and Purdy, 1972). In principle, the lines could be randomly placed with respect to the surfaces of interest. For anisotropic microstructures, the number of intersections of a set of test lines, with the boundaries of microcracks, depends on the angular orientation of the test lines in the plane. Thus, in order to obtain a representative average value of the intersection count, it is important to perform the measurements on different angular orientations in the cross-section under interrogation. The dependence of the number of intersections per unit length with the angle of the test lines can be used to characterize the degree of microcracking anisotropy. We applied a set of test lines to the cross-sections at 0, 30, 45, 60, 90, 120, and 135°, with respect to the impact direction, and evaluated P_L separately for each angle θ. Total crack surface area per unit volume, S_v, was determined from P_L. Plotting S_v vs. θ, provides a so-called space rosette, which reflects the degree of preferred orientation. The rosette is a circle for specimens in which microcracking has no preferred orientation.

To characterize the fragment size at different material points, a mean intercept length approach was used. This procedure is based on the counting of line intersections with the fragments' boundaries. It utilizes a 50 cm total length circular pattern consisting of three concentric circles whose radii obey an

Table 2
Summary of penetration experiments

Shot no.	Ceramic	Impact velocity (km/s)	Interface defeat	Entrance hole (mm)	Exit hole (mm)
7-1797	Ebon-A Al_2O_3	1.7 ± 1	Partial	8.90	8.90
7-1798	TiB_2	1.7 ± 1	Partial	11.10	11.10
7-1799	Ebon-A Al_2O_3	1.5 ± 1	Complete	11.24	–
7-1800	TiB_2	1.5 ± 1	Complete	12.00	–
7-1801	Ebon-A Al_2O_3	1.5 ± 1	Complete	11.04	–
7-1802	TiB_2	1.6 ± 1	Partial	9.50	9.50
7-1803	TiB_2	1.5 ± 1	Complete	10.37	–
7-1804	Ebon-A Al_2O_3	1.5 ± 1	Partial	9.65	7.65

arithmetic progression (Pellisier and Purdy, 1972). A number of selected areas of the specimen were used to count fragment size as a function of position within the ceramic cross section. The average length of the fragments is defined by $L = 1/P_L$ in which P_L represents the number of line intersections with the fragment boundaries.

3. Results and discussion

Stress histories recorded at the second interface between the lower surface of the ceramic disk and top of the bottom steel plate from shots 7-1797 and 7-1800 are shown in Fig. 6. The strain gauge profile exhibited zero strain until the shock wave approached the gauge location. The stress profile for shot 7-1800 shows a progressive stress increase in the form of a ramp to about 0.8 GPa over a period of 30 μs. Then the axial stress decays and increases once more until the gauges fail. In experiment 7-1797, the axial stress rises to a value of about 1 GPa in approximately 10 μs. This time corresponds to the failure of the gauges. The difference in stress increase, between experiments 7-1797 and 7-1800, appears to be related to the fact that in experiment 7-1797 full penetration occurred, while in experiment 7-1800 the penetrator is defeated at the ceramic-cover plate interface. The stress and strain gauges in experiment 7-1797 failed due to the penetrator arrival at the gauge location. In experiment 7-1800, the failure of the gauges is presumed to be the result of the strong shock wave and resulting interface motion.

Fig. 7 shows the back plate free surface velocity recorded by VISAR in shots 7-1799, 7-1800, and 7-1803. This velocity history represents the early part of the target motion as inferred from numerical simulations (see e.g. Espinosa et al., 1998). In experiments 7-1800 and 7-1803 the initial increase in free surface velocity is likely due to the waves generated by the WHA rod during penetration through the cover plate. As the WHA penetrator is defeated at the ceramic-cover plate interface, through penetrator lateral flow, the velocity drops to low velocity values. The measured values of in-situ stress and velocity histories during ballistic penetration are key parameters to compare against numerically predicted stress and velocity histories.

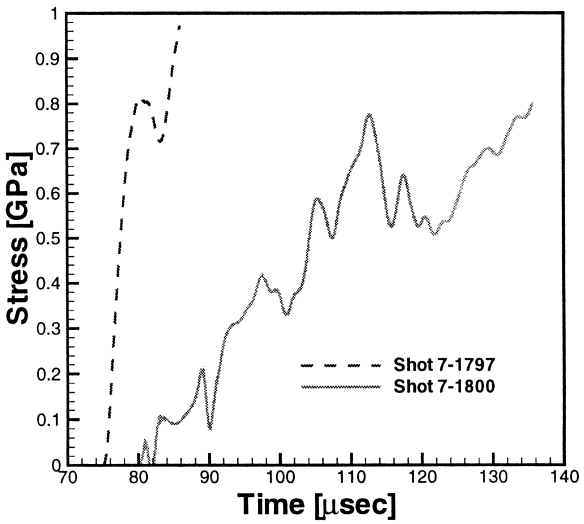

Fig. 6. Stress histories from shots 7-1797 and 7-1800.

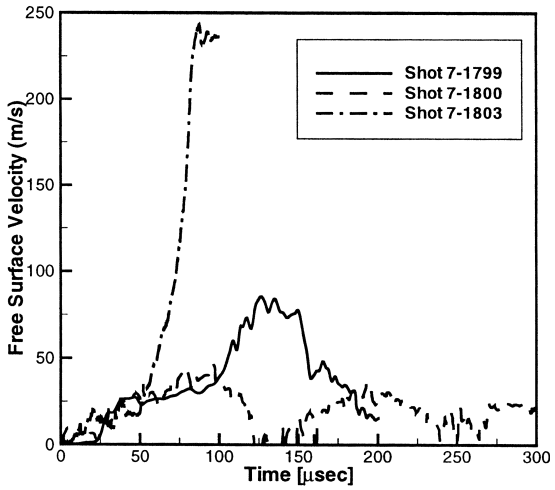

Fig. 7. Back plate free surface velocity histories from shots 7-1799, 7-1800, 7-1803.

Optical and scanning electron microscopic observations were made on recovered ceramic and ceramic/penetrator mixture specimens from the post shot targets. In shots 7-1797 and 7-1798 the penetrator was partially defeated by lateral flow at the ceramic-graphite interface. However, the WHA long rod was able to completely penetrate the target. Pictures of entrance and exit holes are shown in Figs. 8 and 9. Pictures of the top and bottom alumina surfaces are shown in Figs. 10 and 11. The top view shows a crater left by a portion of ceramic bonded to the cover plate, by melted WHA, and a ring of graphite. In the center of the picture, a disk of infiltrated epoxy can be observed. This epoxy was infiltrated prior

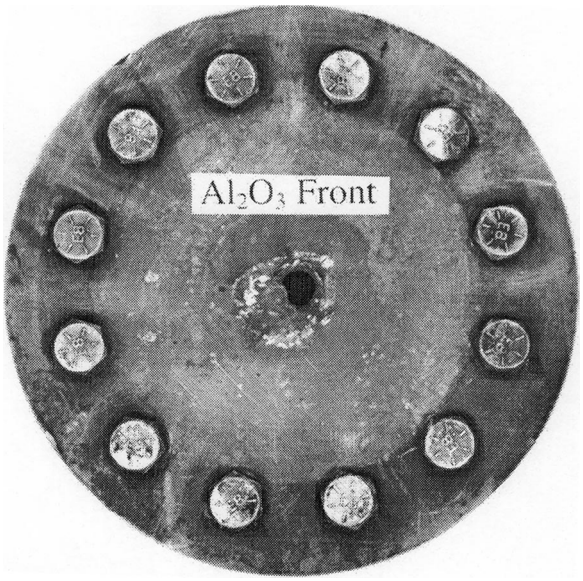

Fig. 8. Photograph of the top surface of recovered steel cover plate from experiment 7-1797 (Al_2O_3 ceramic).

Fig. 9. Photograph of the bottom surface of recovered steel back plate from experiment 7-1797 (Al_2O_3 ceramic).

to the disassembly of the target. Fig. 11, shows the fragmentation pattern at the bottom of the ceramic plate. A well defined pattern of radial and circumferential cracks are observed. The recovered alumina ceramic disk, that matches the crater previously mentioned, exhibits a well defined layered structure of tungsten alloy entrapped in alumina ceramic fragments at different depths along the penetrator cavity (Fig. 12). It can be observed, in this figure, that the interface between alumina and steel has a thin layer of WHA, in which thickness decreases with distance from the central hole. A second layer of WHA is observed at the bottom of the alumina. Moreover, tungsten penetrator material is embedded in the

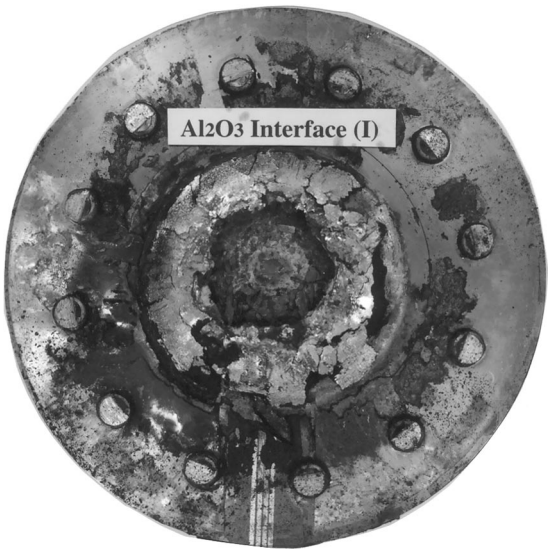

Fig. 10. Photograph of the top surface of recovered Ebon-A Al_2O_3 disk from experiment 7-1797.

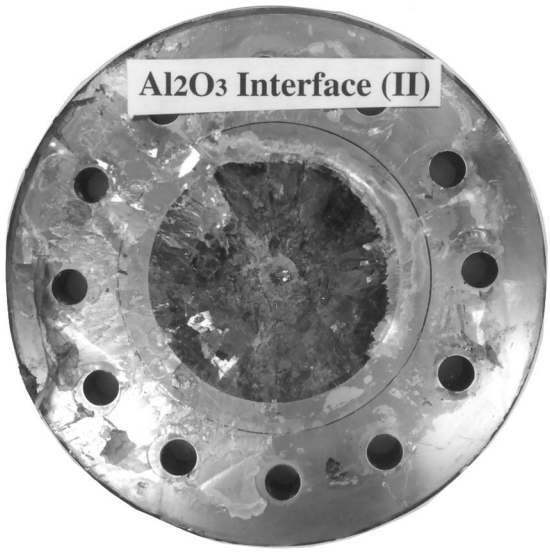

Fig. 11. Photograph of the bottom surface of recovered Ebon-A Al_2O_3 disk.

cracked ceramic as shown in Fig. 13. Also seen in this micrograph are elongated tungsten grains resulting from accumulation of shear deformation. The extent of grain distortion decreases with distance from the crater hole made by the penetrator. The overall deformation picture described in this paragraph is defined as *partial interface defeat*. In other words, when the penetrator flows laterally, at the interface between cover plate and ceramic, but still continues to penetrate the ceramic and back plates, we use the term partial interface defeat.

Optical micrographs, shot 7-1798, taken from the lower face of the top steel plate and upper face of the bottom steel plate are shown in Figs. 14 and 15. The lower face of the top steel plate shows the

Fig. 12. Section of the recovered top portion of alumina disk, from shot 7-1797, welded to the steel cover by melted tungsten heavy alloy penetrator material. The section shows lateral flow of tungsten heavy alloy material at various depths.

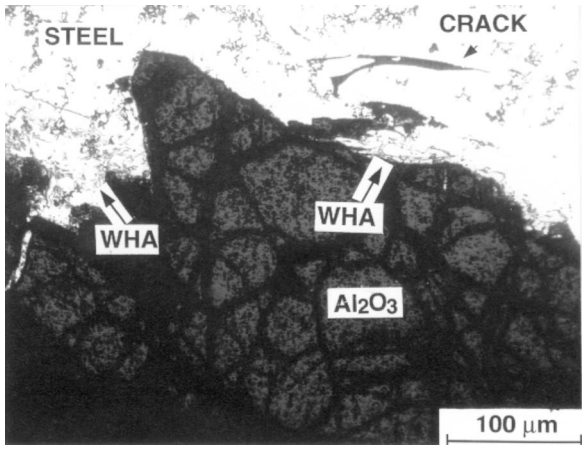

Fig. 13. High magnification micrograph of recovered material, from shot 7-1797, at the ceramic-cover plate interface. The micrograph shows heavily deformed WHA penetrator, fragmented alumina indenting the steel cover plate and shear localization and crack formation in the steel cover plate.

lateral spread of graphite towards the bolts, see Fig. 14. The partial defeat of the penetrator is seen from the traces of melted WHA material left on the face as a result of the lateral flow. The upper face of the bottom steel plate, shown in Fig. 15, shows the failed stress and strain gauges. Marks left by the fragmented TiB_2 and total penetration of the plate are also seen.

Optical micrographs taken from the recovered TiB_2 ceramic disk, shot 7-1798, are shown in Figs. 16–18. The top surface of the TiB_2, shown in Fig. 16, exhibits substantial tungsten penetrator material which flowed laterally at the graphite–ceramic interface. The WHA penetrator material has the shape of a thin dish with a hole in the middle. Once again, this is evidence of partial interface defeat as

Fig. 14. Photograph of bottom surface of recovered cover plate from shot 7-1798.

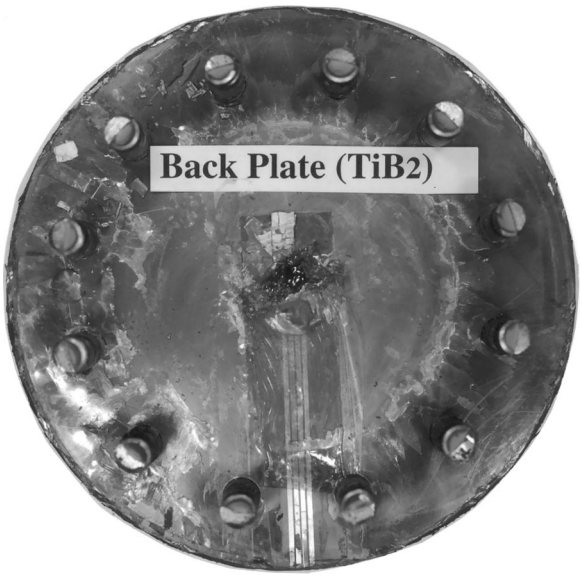

Fig. 15. Photograph of top surface of recovered back steel plate from shot 7-1798.

previously defined. A radial crack pattern at the back surface of the TiB_2 disk is shown in Fig. 17. A cross-section of the sliced TiB_2 disk is shown in Fig. 18. The picture reveals relatively large ceramic fragments and a large chunk of WHA from the rear of the penetrator.

Quantification of crack surface per unit volume and fragment size, as a function of position, was performed on a region of the cross section shown in Fig. 18. A magnified view of the region chosen for

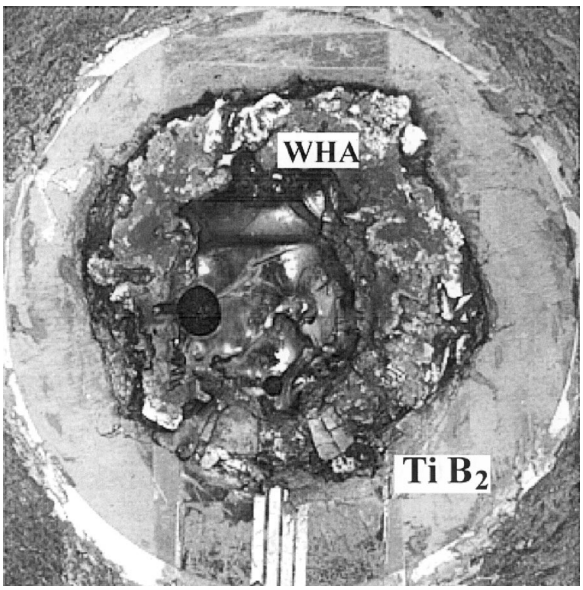

Fig. 16. Photograph of top surface of recovered TiB_2 disk from shot 7-1798. Partial interface defeat is put in evidence by formation of a thin sheet of WHA material at the ceramic-cover plate interface.

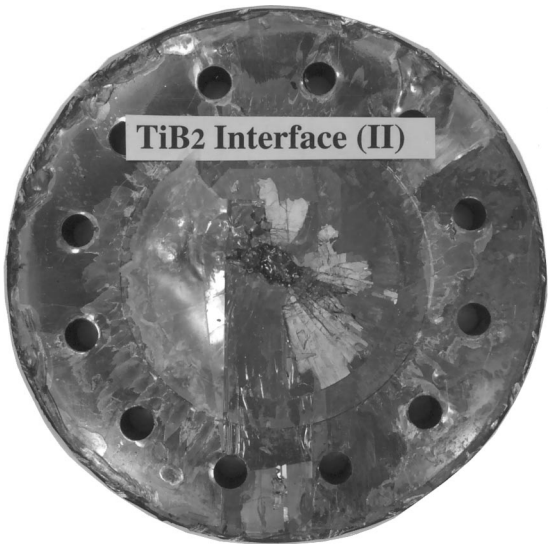

Fig. 17. Photograph of the bottom surface of recovered TiB_2 disk from shot 7-1798. Radial and circunferential cracks are clearly seen.

quantification is shown in Fig. 19. Measured crack surface area per unit volume in the TiB_2 disk recovered from shot 7-1798, as a function of distance from the crater, is plotted in a rosette form in Fig. 20. As seen in this plot, a rotation of the orientation in which S_v is maximum, in each rosette, suggests a change in preferred orientation of the macrocracks. The reduction of S_v maximum, in the various rosettes, reveals that the crack density decreases with distance from the penetrator crater. The fragment size distribution in TiB_2 from this shot, as a function of distance from the crater center, is shown in Fig. 21. Fragment sizes were evaluated at three depths, 2.3, 5.0, and 7.7 mm from the ceramic top surface (see Fig. 18), in order to assess damage in the interior of the ceramic. It is evident from the data shown in Fig. 21 that fragment size increases with distance from the crater, which is generally true in most brittle targets. Fragment size also increases with depth from the ceramic top surface indicating that the ceramic interior is less damaged compared to the surface. Both of these observations and

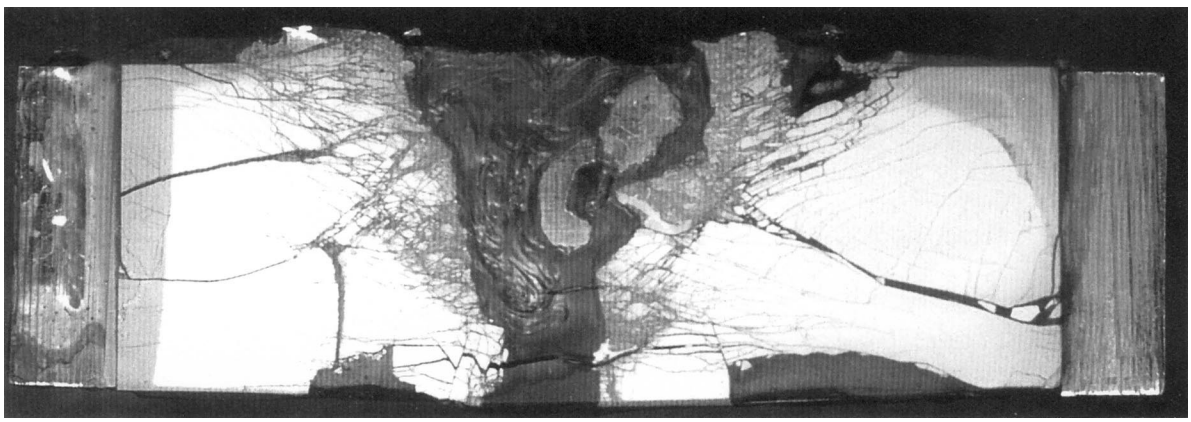

Fig. 18. Cross-section of the sliced TiB_2 disk from shot 7-1798 showing full penetration of the TiB_2 plate.

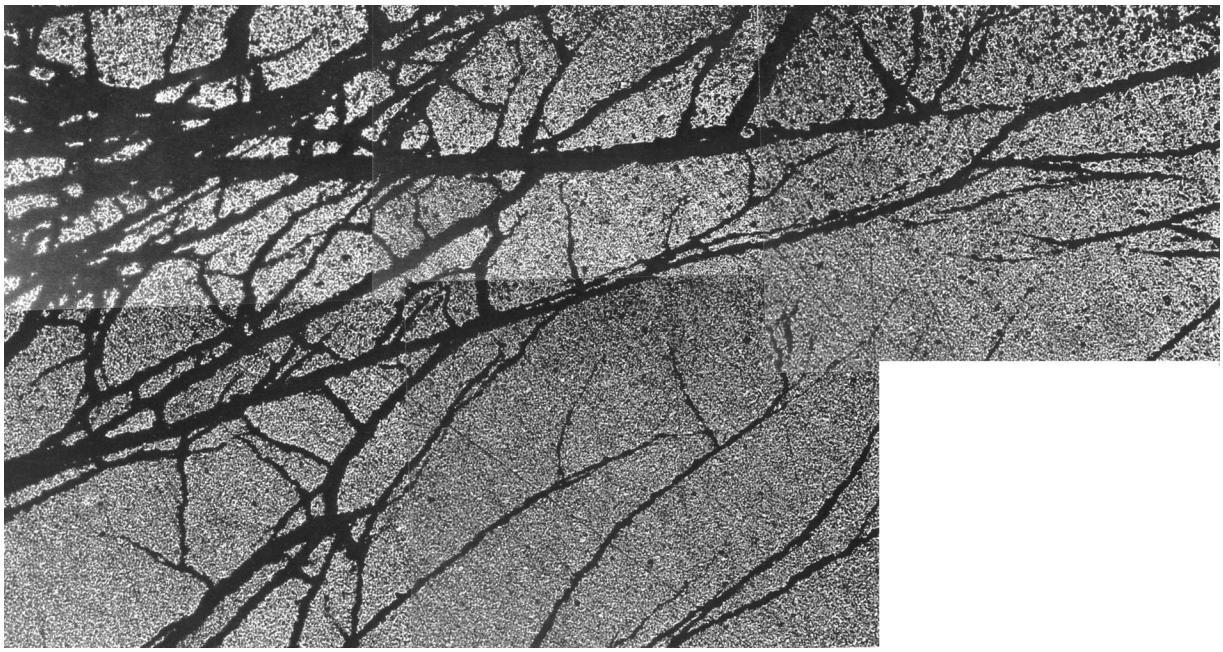

Fig. 19. Optical micrograph used to quantify crack surface area per unit volume.

measurements of fragment size distribution can be used to check the accuracy of numerical simulations of the penetration process.

Complete interface defeat of the WHA penetrator was achieved in shots 7-1799 and 7-1800. The 4340 steel cover plates in both shots were heat treated to a hardness of $Rc = 53 \pm 1$. The improved ballistic performance of these two targets compared to those of 7-1797 and 7-1798 is thought to be due to a combination of three factors: (i) greater hardness of the cover steel plate compared to that in shots 7-1797 and 7-1798, (ii) welding of the cover and bottom plates to the middle plate containing the ceramic,

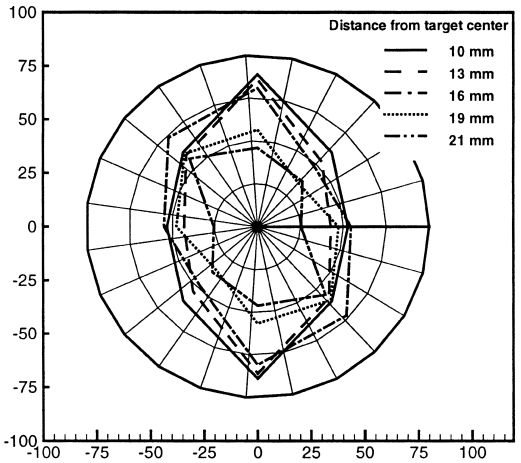

Fig. 20. Crack surface area per unit volume rosette. Preferred crack orientation is inferred from the lack of center symmetry.

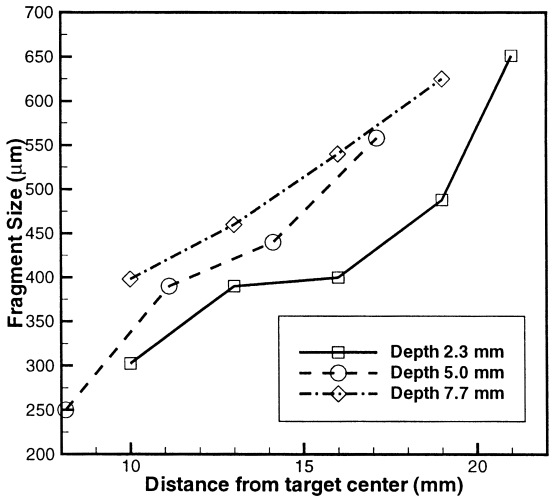

Fig. 21. Variation of fragment size with distance from target center.

i.e., increased stiffness of the target assembly, and (iii) absence of the low shear strength epoxy (used to glue the gauges) at the two interfaces between the three target disks in target 7-1799 and the top interface in target 7-1800. Stress wave reflections from the low impedance epoxy bonds may subject the ceramic to tensile release waves and premature damage. In this context one should note that Hauver et al. (1994) did not have any epoxy bonds in their target assembly which achieved complete interface defeat of WHA penetrators. The epoxy bonds in our target assembly were used to embed stress/strain

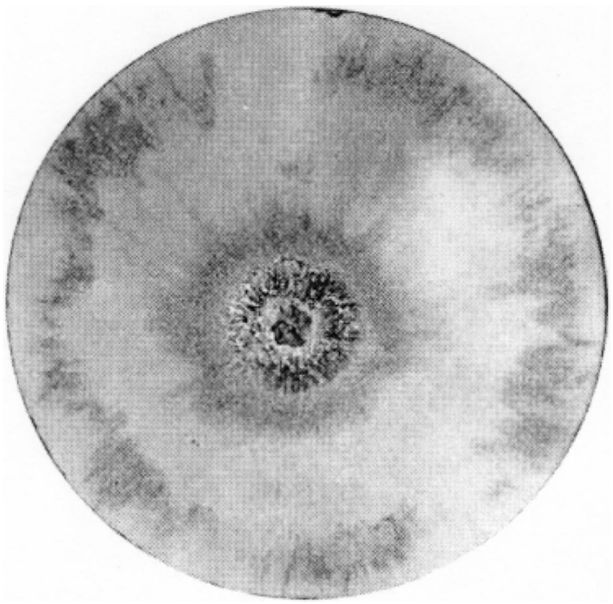

Fig. 22. Photograph of the top surface of recovered TiB_2 disk from experiment 7-1800. Marks from the lateral flow of WHA material are observed. This indicates ceramic wear due to the high pressure and sliding velocity.

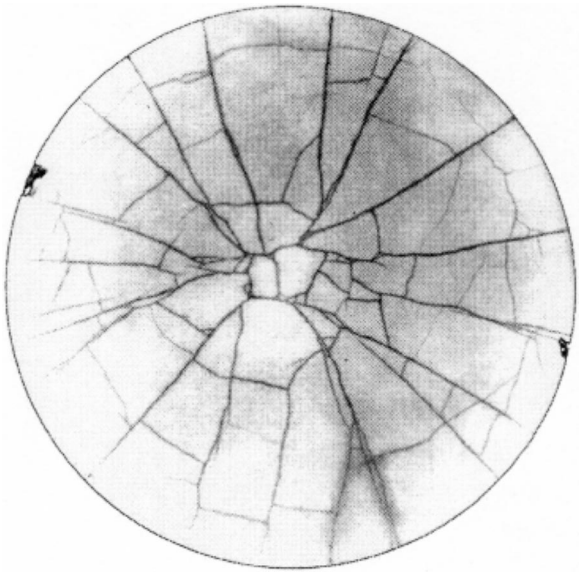

Fig. 23. Fragmentation pattern at the bottom surface of recovered TiB_2 disk.

gauges at the interfaces in order to measure in-situ stress/strain history during ballistic penetration. The intent was to measure stress/strain values that can be compared to numerically simulated values.

The recovered TiB_2 ceramic disk from target 7-1800, shown in Figs. 22 and 23, was intact with a dark circular region in the center, where the WHA penetrator impinged and flowed laterally. Optical observations on the back surface of TiB_2 showed a star burst pattern of linear cracks radiating outward

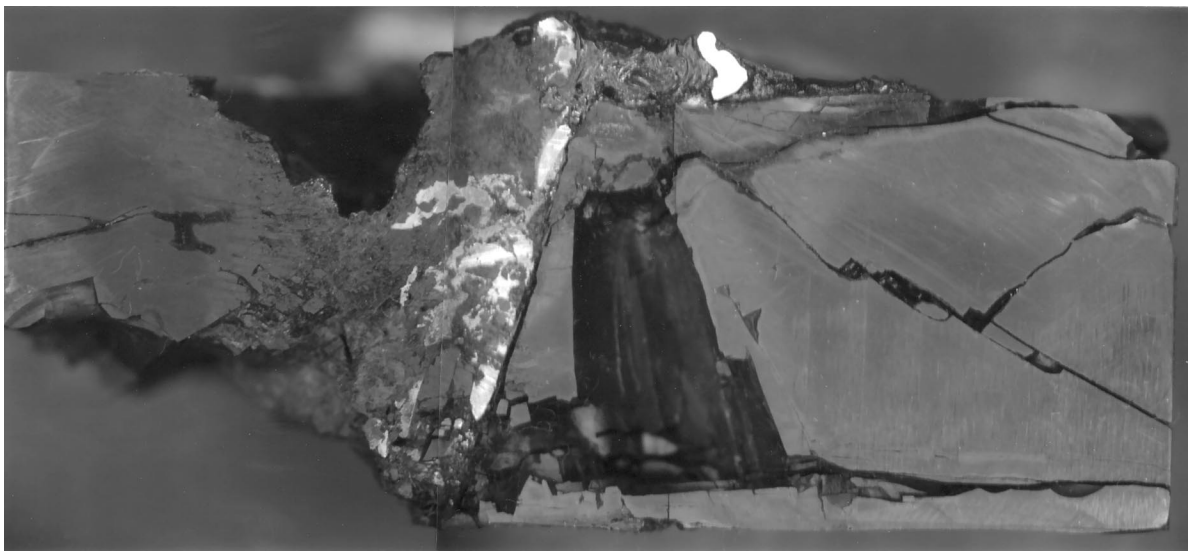

Fig. 24. Cross-section of the sliced Ebon-A Al_2O_3 disk from, shot 7-1801, showing interface defeat of the long rod WHA penetrator. Note that the WHA material is mixed with ceramic fragments asymmetrically.

from the center. These linear cracks may have been produced by tensile waves reflected from the circular periphery of the target assembly.

The recovered alumina disk from target 7-1801 exhibited a crater along with radial and circumferential cracks originating from the crater as shown in Fig. 24. The extent of damage to the alumina disk was relatively extensive compared to that in the TiB_2 disk. This difference in the ballistic performance of the two ceramics is due to the superior compressive and fracture properties of TiB_2. Further observations on the orthogonal views of the crater and lateral crack patterns, on sectioned surfaces of the alumina disk, showed a cone configuration similar to the crack pattern observed in ceramics and glasses subjected to static indentation. Target 7-1801 was assembled in exactly the same way as target 7-1799, except that the graphite disk was only half as thick in 7-1801 (1.3 mm) compared to that in 7-1799 (2.38 mm). Another difference is that, the welding of target 7-1801 was done at UDRI with a different wire welder. We did achieve complete interface defeat of the penetrator in this shot like in 7-1799, but the damage to the alumina ceramic was much more severe. The penetrator produced a relatively larger crater and tungsten fragments are further embedded into the ceramic as shown in Fig. 24. The diminished ballistic performance of alumina in this shot may be the result of two different factors: (i) variation in target assembly and (ii) thinner graphite disk. The relatively soft and porous graphite disk with negligible shear strength on top of the hard ceramic induces shear failure of the penetrator and accommodates the sheared penetrator material. Furthermore, the lateral flow of WHA provides a compressive traction on the ceramic surface and therefore it assists ceramic confinement. It is also possible that the 2.38 mm thick graphite disk in target 7-1799 provided optimum free volume to accommodate sheared tungsten in between the top of the ceramic and the cover steel plate. It is possible that the free volume in the thinner graphite disk (1.3 mm), in shot 7-1801, was not enough to accommodate all the sheared penetrator fragments between the top of the alumina ceramic and the cover plate and consequently, the excess material ended up embedded in the alumina ceramic disk.

The configuration and the dimensions of the three plates comprising targets 7-1802 and 7-1803 were exactly the same as in target 7-1800. In target 7-1802, the hardness (Rc) of the cover plate was 30 whereas in 7-1803 it was 51. This difference in the hardness of the cover plate dramatically affected the

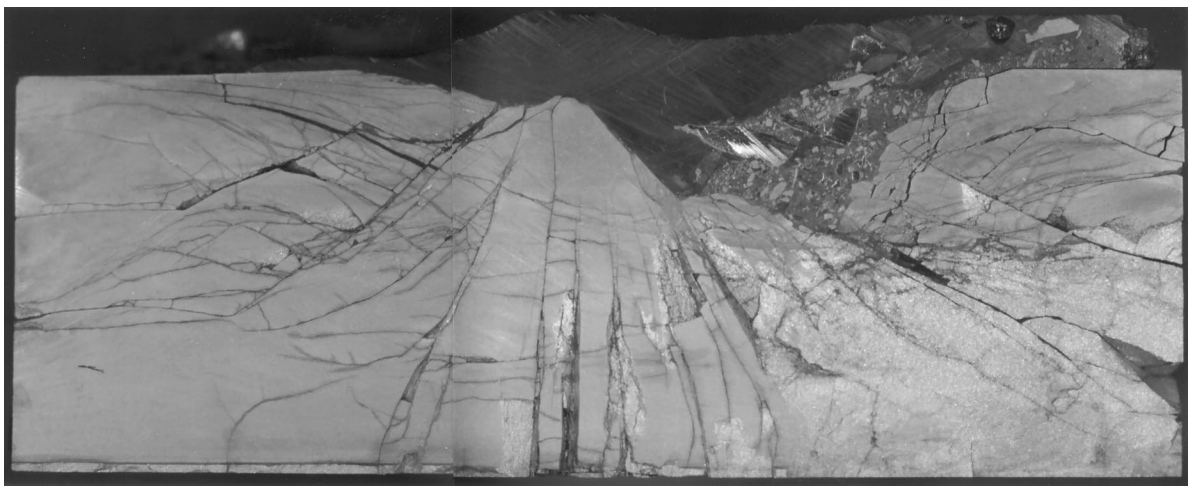

Fig. 25. Recovered TiB_2 disk from shot 7-1803 showing more damage compared to that in experiment 7-1800. Mixing of WHA material with TiB_2 fragments is less pronounced than in the case of the Al_2O_3 target.

ballistic performance of the two targets; 7-1802 was completely penetrated and complete interface defeat was achieved in target 7-1803. The damage to the TiB_2 ceramic in 7-1803 was, however, more severe than that of the TiB_2 ceramic in 7-1800, where the ceramic was almost intact with only a few radial cracks. A cross-section of the TiB_2 ceramic in shot 7-1803 is shown in Fig. 25. It is possible that wave reflection from the epoxy layer used to embed the stress/strain gauges, at the second interface, subjected the ceramic to tensile release waves, thereby damaging it before the arrival of the penetrator. Target 7-1800, with no epoxy bonds between the plates, defeated the penetrator completely through interface WHA lateral flow with very little ceramic damage (see Figs. 22 and 23).

The configuration of the three plates comprising target 7-1804 was exactly the same as in 7-1799 with the difference that the bottom 4340 steel plate was only 19 mm thick instead of 25 mm. Only partial interface defeat of the penetrator was achieved in 7-1804 possibly due to the thinner bottom plate. In target 7-1799, the penetrator was completely defeated. The thickness of the bottom plate in similar targets prepared by Hauver et al. (1993, 1994) was much greater than 25 mm and they achieved complete interface defeat. The different ballistic performance observed in shots 7-1799 and 7-1804 clearly suggests that in order to achieve complete interface defeat, the bottom 4340 steel plate has to be at least 25 mm thick. This translates into a minimum plate stiffness when the boundary conditions of the back plate are taken into account.

4. Conclusions

We next itemize a series of conclusions which can be drawn from the experimental features previously discussed. Special emphasis is placed on local (e.g., hardness, shear resistance) versus global (e.g., cover plate stiffness, back plate stiffness) behavior of the multi-layered target system.

1. Tungsten long rods shot at 1.5 km/s can be completely defeated through the interface defeat mechanism by stiff multi-layered alumina and TiB_2 ceramic targets (see also Bless et al. (1992) and Hauver et al. (1993)). The overall stiffness of the multi-layered ceramic target assembly is improved by welding the cover and bottom disks to the middle disk containing the 25 mm thick TiB_2 and Ebon-A alumina ceramic disks. Recovered TiB_2 ceramic disks, from the post-shot targets in which total interface defeat occurred, showed very little damage. In the case of the alumina disks, there was a shallow crater at the impact site with radial cracks originating from the crater.
2. Ballistic performance of a multi-layered ceramic target depends very strongly on the hardness of the cover steel plate. Cover steel plate hardness of $Rc = 53$ appears necessary for interface defeat (see also Hauver et al., 1993).
3. Waves generated as a result of interface reflections from low shear strength epoxy bonds, between the three disks comprising the target, enhanced ceramic damage and thereby diminished its ballistic performance.
4. A critical threshold velocity for failure mechanism transition from defeat to complete penetration is apparent from the experimental results (see also Hauver et al. (1993) and Subramanian and Bless (1995)).
5. The stiffness of the back plate must be high enough to prevent ceramic bending and wave damage.
6. The stiffness of the cover plate must be such that excessive plate bulging and loss of ceramic confinement in the neighborhood of the so-called Mescal zone (highly fragmented region) does not occur. Otherwise, partial interface defeat may result.
7. The experimental observations show that there are local and global features that affect the overall target performance. Local effects are related to the materials performance, viz., cover plate hardness and shear resistance of the fragmented ceramic. Global effects are related to structural features.

Overall stiffness of cover and back plates, as a function of boundary conditions and thickness, appear to play a major role in the transition from interface defeat to ceramic erosion mechanisms. The type of ceramic appears less relevant. In fact, it can be inferred that most ceramics can achieved interface defeat at a low enough velocity. Hence, ceramic HEL can be correlated with the value of the critical threshold velocity for failure mode transition, see Section 4.

8. Scaling rules (for full field applications) can be derived by preserving cover/back plate stiffness, ratio between penetrator volume and graphite disk volume, materials hardness and toughness, and porosity of the graphite layer to the experiments reported in this work in which total interface defeat occurred. An estimate of the plate stiffness can be made by considering simply supported plates in the case of bolted plates and plates with fixed boundaries in the case of welded targets. Standard plate theory can be used to compute its stiffness.

Due to the complexity of the problem examined in this work and the interrelation between the various design parameters, future research should focus on numerical simulations of the event with material models independently validated. Understanding of the relevance of each design parameter can be then achieved by performing a series of simulations in which only one parameter is changed in each simulation (see e.g. Espinosa et al., 1998) In this regard, the damage quantification and the material stresses and velocity histories provided in this work can be used as constraints to be satisfied by numerical simulations of the ballistic penetration event.

Acknowledgements

The authors would like to thank George Hauver for sharing details of the experimental configuration used in his research as well as the insight provided through many discussions. A special thank is due to Ed Rapacki for providing WHA penetrators used in this investigation. Mark Laber is thanked for his help with the experimental effort. This research was supported by the Army Research Office through MURI Grant No. DAAH04-96-1-0331.

References

Bless, S., Ben-yami, M., Apgar, L., Eylon, D., 1992. Impenetrable targets struck by high velocity tungsten long rods. In: Proc. 2nd Int. Conf. on Structures under Shock and Impact, Portsmoutkh, UK.

Charest, J., 1997. personal communication.

Espinosa, H.D., Clifton, R.J., 1991. Plate impact experiments for investigating inelastic deformation and damage of advanced materials. In: Kim, K.S. (Ed.), Symp. on Experiments in Micromechanics of Fracture-Resistant Materials, ASME Winter Annual Meeting, Atlanta, GA, pp. 37–56.

Espinosa, H.D., Dwivedi, S., Zavattieri, P.D., Yuan, G., 1998. Numerical investigation of penetration in multilayer material/structure systems. Int. J. Solids and Structures 35 (22), 2975–3001.

Hauver, G., Netherwood, P., Benck, R., Kecskes, L., 1993. Ballistic performance of ceramic targets. In: Proc. of Army Symposium on Solid Mechanics, Plymouth, MA, USA.

Hauver, G., Netherwood, P., Benck, R., Kecskes, L., 1994. Enhanced ballistic performance of ceramics. In: Proc. 19th Army Science Conference, Orlando, FL.

Hauver, G., 1997. personal communication.

Klopp, R.W., Shockey, D.A., 1991. The strength behavior of granulated silicon carbide at high strain rates and confining pressure. J. Appl. Phys 70 (12), 7318–7326.

Pellisier, G.E., Purdy, S.M., Co-Chairmen, 1972. Stereology and quantitative metallography. ASTM Special Technical Publication 504. Amer. Soc. for Testing and Mats., Philadelphia.

Rapacki, E., Hauver, G., Netherwood, P., Benck, R., 1996. Ceramics for armors — a material system perspective. In: Proc. 7th Annual TARDEC Ground Vehicle Survivability Symposium.

Sairam, S., Clifton, R.J., 1994. Pressure-shear impact investigation of dynamic fragmentation and flow of ceramics. In: Gilat, A. (Ed.), ASME AMD-Vol. 197, Mechanical Testing of Ceramics and Ceramic Composites, pp. 23–40.

Shockey, D.A., Marchard, A.H., Skaggs, S.R., 1990. Failure phenomenology of confined ceramic targets and impacting rods. Int. J. Impact Engng 9 (3), 263–275.

Subramanian, R., Bless, S.J., 1995. Penetration of semi-infinite AD995 alumina targets by tungsten long rod penetrators from 1.5 to 3.5 km/s. Int. J. Impact Engng 17, 817–824.